Ceramics International 47 (2021) 25105–25120

Contents lists available at ScienceDirect

Ceramics International

journal homepage: www.elsevier.com/locate/ceramint

High temperature resistant fly-ash and metakaolin-based alkali-activated foams

Katja Traven [a], Mark Češnovar [a,b], Srečo D. Škapin [c], Vilma Ducman [a,*]

[a] Slovenian National Building and Civil Engineering Institute (ZAG), Dimičeva 12, 1000, Ljubljana, Slovenia
[b] International Postgraduate School Jožef Stefan, Jamova 39, 1000, Ljubljana, Slovenia
[c] Jožef Stefan Institute, Jamova 39, 1000, Ljubljana, Slovenia

ARTICLE INFO

Keywords:
Alkali-activated foams
Fly-ash
Porosity
Thermal stability
Mechanical properties
Microstructural analysis

ABSTRACT

Alkali-activated foams (AAFs) present one of the most promising materials for use in the construction sector. Their main advantages lie in their utilization of waste material and their ability to form at temperatures well below 100 °C, while still competing in performance with foamed glass or ceramics. The present body of research has focused on improving the thermal stability of fly-ash foams by i) adding metakaolin, and ii) changing the activator from sodium-based to potassium-based components. It has been confirmed that a certain increase in thermal resistance is achieved through the addition of metakaolin while changing activators played a crucial role. While sodium-based AAFs without metakaolin start to shrink at approximately 600 °C, samples that have had metakaolin added start to shrink at approximately 700 °C. Samples without metakaolin that have used a potassium activator start to shrink at approximately 800 °C, whereas potassium-based samples with the addition of metakaolin start to shrink at approximately 900 °C.

1. Introduction

In recent years, there is a growing concern about the vast amounts of energy consumption and environmental pollution, what calls for some urgent actions [1]. Construction sector has been recognised as one of the field which contribute the most to the global warming [2]. Alkali activated materials (AAMs) have thus received significant attention, as they represent promising alternatives to building materials and ceramics. AAMs are aluminosilicate-based binders with the ability to harden at low temperatures (below 80 °C) in a relatively short time (less than 48 h) [3]. They are derived (i) through the reaction of a solid amorphous aluminosilicate powder (precursor) with a liquid alkali metal source (activator) [4] or (ii) by the addition of water to the dry mixture of solid precursor and activator, which is also solidified (also called one-part AAMs) [5]. A wide range of precursors are suitable for the production of AAMs, including metakaolin, fly-ash, clays, various slags, wools, ceramics, and other waste materials [6–13]. Metakaolin (MK) and fly-ash (FA) are two of the most common materials used for the manufacture of AAMs. MK-based AAMs can exhibit good mechanical properties at an early age but are prone to cracking and strength degradation when exposed to elevated temperatures [14]. FA-based AAMs, however, exhibit lower initial strength compared to MK-based AAMs but exhibit better performance at high temperatures, due to a large number of small pores that facilitate the escape of moisture when heated, thus causing minimal damage to the AAM matrix. The increase in strength is also partially ascribed to the sintering process of un-reacted fly-ash particles [15]. Due to the diversity of suitable precursors, AAMs could be designed to have superior properties compared to conventional binders [16], and when waste material is used as a precursor/activator and a low-temperature process is adopted a reduction in the CO_2 footprint of the process can also be achieved, especially when one-part AAMs are produced [17].

AAMs are being considered for numerous products which can be obtained from the alkali activation process (such as paving stones, blocks, curbs, slabs, partitions, refractory materials, materials for specific industrial applications, and so on), and they could replace traditional construction products. Among them, alkali-activated foams (AAFs) present one of the most promising materials, finding applications as adsorbents, catalysts, bone scaffold materials, filtration membranes, and thermal/acoustic insulators [18,19]. A further advantage is that they can be formed at temperatures well below 100 °C while possessing properties similar to foamed glass or ceramics, both of which are produced at greatly elevated temperatures (above 900 °C).

There are several approaches to the formation of AAFs: i) sacrificial

* Corresponding author.
E-mail address: vilma.ducman@zag.si (V. Ducman).

https://doi.org/10.1016/j.ceramint.2021.05.241
Received 23 March 2021; Received in revised form 14 May 2021; Accepted 24 May 2021
Available online 9 June 2021

fugitives, ii) partial sintering, iii) replica templates, iv) additive manufacturing, v) direct foaming, and others. Within direct foaming, which represents the most straight-forward method of obtaining AAFs, air voids can be introduced to a slurry either mechanically, where the pre-made foam is physically incorporated into a slurry of alkali-activated material, or chemically, using foaming agents such as aluminium (Al), SiC, silicon powders, NaOCl, FeSi alloy, sodium perborate, hydrogen peroxide (H_2O_2) [18,20]. The latter, as used in our study, is an inexpensive compound, forming among others a gaseous product (O_2) leading to void formation, meaning a highly porous material can be obtained during the hardening stage. In order to control and stabilize these voids, surfactants or stabilizing agents such as sodium oleate, sodium dodecyl sulfate, Triton, and stearic acid, among others, are also incorporated into the slurry [21,22].

Several studies have proven that, notwithstanding the method or additives used in the production of AAFs, the compressive strength of AAFs decreases with a reduction in density, usually ranging between 1 MPa and 10 MPa with a density of 360–1400 kg/m^3 [23,24]. Ducman and Korat, for example, used two different foaming agents (aluminium powder and H_2O_2) and sodium silicate as activator to obtain highly porous structures with densities ranging between 0.61 and 1.0 g/cm^3 [21]. The resulting compressive strengths ranged from 3.3 to 4.3 MPa when Al powder was added compared to 2.9–9.3 MPa when H_2O_2 was used. Bai et al. developed metakaolin-based foams activated by mixture of K_2SiO_3 and KOH, using hydrogen peroxide as a foaming agent and various oils (sunflower, olive, vegetable, canola) as surfactants. The lowest density of the foams obtained was 0.37 g/cm^3 and the compressive strength at that density was 0.3 MPa [25]. Medri et al. investigated lightweight composite panels, using expanded vermiculite as a lightweight aggregate, potassium based activator and hydrogen peroxide as the foaming agent. The densities ranged between 700 and 900 kg/m^3, while the average strength was approximately 2 MPa [26]. Hajimohammadi et al. made metakaolin-based AAFs, also using hydrogen peroxide as a foaming agent and sodium water glass as activator. They reported foams of density 400–550 g/cm^3 with normalized compressive strengths between 0.2 and 0.8 MPa [27]. Using chemical foaming and sodium-based activator Wu et al. successfully prepared ultra-lightweight foamed geopolymers (UFG) based on fly-ash and metakaolin with densities between 150 and 300 kg/m^3. Despite the low densities, the geopolymers exhibited relatively high compressive strengths of up to 2.2 MPa [28].

To provide further context to this study, some studies investigating the resistance of AAMs to harsh conditions, such as exposure to elevated temperatures, will be summarized. Thermal stability is a valuable performance characteristic to ensure safe usage within a certain temperature range. Unlike conventional building materials such as Ordinary Portland cement (OPC), which irreversibly degrades in strength above 200 °C due to decomposition of the main binding phases (CSH, $Ca(OH)_2$ and others) and water loss [29], alkali-activated materials have been shown to exhibit great potential as fire-resistant materials in civil engineering [23,30–32]. Lahoti et al. investigated metakaolin-based geopolymers activated with sodium silicate activator and subjected to elevated temperatures and showed that all specimens (differing in the Si/Al molar ratio) experienced a reduction in compressive strength after exposure to high temperatures (up to 900 °C), together with poor volume stability at mesoscale with very high thermal shrinkage [33]. Fan et al. studied the thermo-mechanical properties of geopolymers prepared using a class F fly-ash activated with potassium silicate. The results showed that, when cured under appropriate conditions, the geopolymer could reach good compressive strengths (over 100 MPa) as well as good residual strength after exposure to 500 °C (up to 96 MPa) [34]. Guerrieri et al. conducted a study on sodium-based alkali-activated slag pastes (AASP) and showed that they had a rapid strength loss of 60% between 100 and 200 °C, 30% at 800 °C, and the total strength loss accrued at 1200 °C [35]. Fewer experimental results, however, were found concerning the thermal performance and fire resistance of foamed alkali-activated materials. Cheng-Yong et al. presented a comparative study of un-foamed and foamed geopolymers activated with sodium water glass after exposure to high temperatures and concluded that lightweight AAMs behave differently to unfoamed AAMs in terms of compressive strength when exposed to temperatures up to 1200 °C [29]. Zhang et al. indicated an increase in strength after exposing sodium-based FA-based AAMs to temperatures up to 800 °C [36]. Abdulkareem et al. on the other hand, observed an increase in the strength of lightweight aggregate geopolymer concrete (LWAGC) only up to 300 °C, while between 400 and 800 °C the strength of the material started to deteriorate, even though the sodium-based activators were used for the activation in this case [37]. Badanoiu et al. observed an increment in volume when they exposed glass cullet and red mud-based AAFs to temperatures between 600 and 800 °C [38]. According to Skvara et al. a decrease in the compressive strength of FA-based AAFs activated with the Na_2SiO_3/NaOH mixture was detected after exposure to temperatures up to 800 °C, whereas an increase in the compressive strength was observed after heating to 1000 °C due to sintering of the material [39]. Hlavaček et al. also reported high thermal resistance at elevated temperatures associated with high shrinkage and the effect of sintering [40]. Regarding the cation type, it has also been shown that it affects the incorporation of Al into the framework of geopolymer, with preferential incorporation of potassium into the framework [41]. Nature of the alkali cation also contributes to the level of reaction of the solid aluminosilicate source, as well as to the level of Al incorporation [42]. Which and to what extent phases crystallize during and after the heating is also a very important parameter to be observed. In the alumosilicate system, where potassium is used as an activator, it was reported that leucite crystallized as the major phase after being heated to >1000 °C what improves refractory properties [3]. Korat and Ducman [43] have confirmed the presence of nepheline, sodalite, tridymite, and gehlenite in various fly-ash based foams activated by sodium activators.

In the present study, alkali-activated fly-ash and metakaolin-based foam materials were developed and characterized after curing at room temperature, and after firing at elevated temperatures (600, 800, 1000, and 1200 °C), to develop a material durable at high temperature. Analysis of samples include their mechanical properties before and after exposure to high temperatures, dimensional stability by dilatometric analysis, and thermal resistance through thermogravimetric and differential thermal analysis (TG/DTA) coupled with mass spectrometry (MS). Furthermore, mineralogical and microstructural changes were followed by means of XRD, FTIR, and SEM.

Table 1
Composition of the 2 types of water glass used for the preparation of AAFs (in mass %).

	Na_2SiO_3	K_2SiO_3
SiO_2	30.4	30.1
Na_2O or K_2O	15.4	18.5
H_2O	54.2	51.4

2. Experimental

2.1. Materials

Two types of precursors were used for the preparation of AAFs, namely fly-ash (FA) obtained from a Slovenian thermal plant and metakaolin (MK) produced by Argeco. Two types of water glass were used as activators – sodium silicate (Na_2SiO_3) Crystal 0112 produced by Tennants distribution, Ltd., and potassium silicate (K_2SiO_3) Betol K 5020 T produced by Woellner Austria GmbH. The compositions of each are presented in Table 1. Additionally, NaOH and KOH water solutions (both produced by Donau Chemie, 41.7 mass % water solutions) were used as activators. A 30% hydrogen peroxide solution (produced by Carlo Erba Reagents) was used as a foaming agent and sodium dodecyl

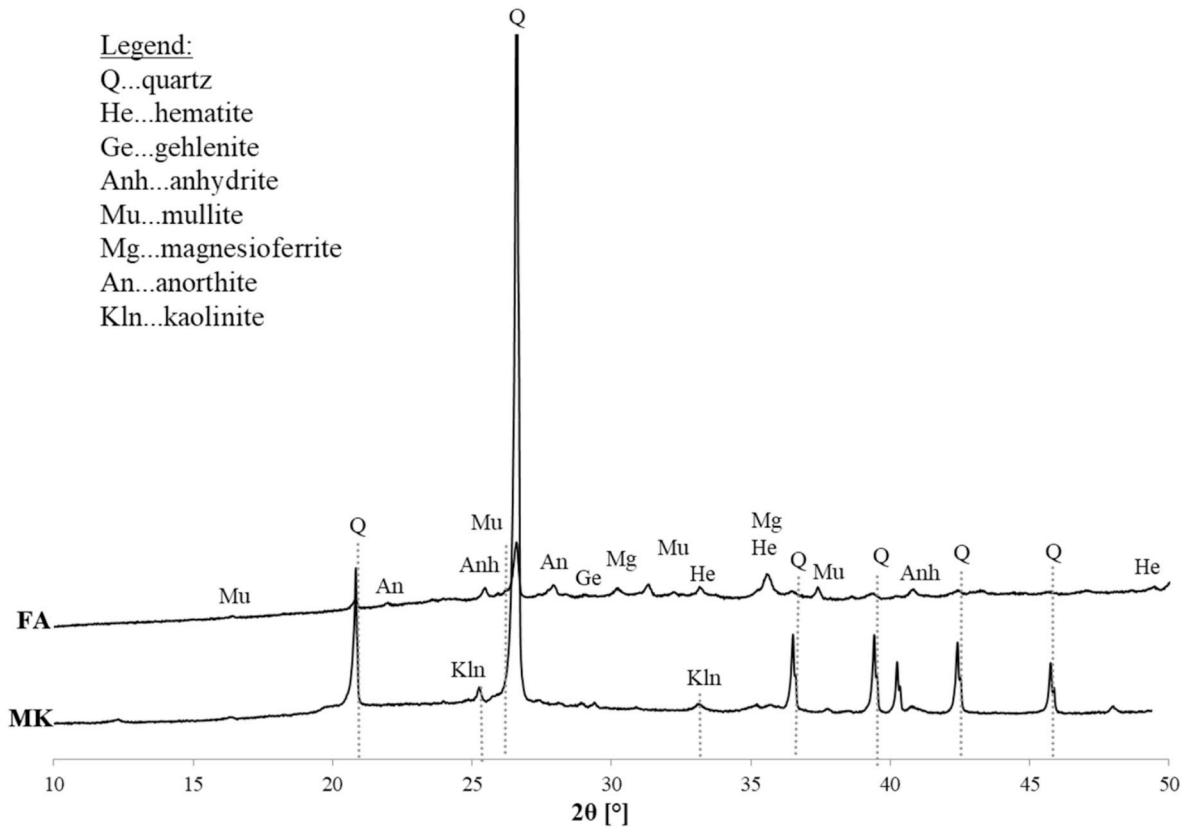

Fig. 1. X-ray diffractograms of fly-ash (FA) and metakaolin (MK).

Table 2
Chemical composition of precursors used for the preparation of AAFs (in mass %; n.d. = not detected).

	LOI	Na_2O	MgO	Al_2O_3	SiO_2	P_2O_5	SO_3	K_2O	CaO	Fe_2O_3	OTH
Fly-ash	0.51	1.19	2.80	22.98	44.82	0.36	0.77	2.20	12.38	10.65	1.34
Metakaolin	2.14	n.d.	0.18	25.30	68.12	0.04	n.d.	0.17	0.43	2.20	1.39

sulfate (produced by Acros organics) as a surfactant.

2.2. Composition of precursors

Firstly, both types of precursors were fully characterized in order to determine their suitability for the alkali-activation process. XRD analysis confirmed that fly-ash (FA) comprised over 70% amorphous phase, making it suitable for the alkali-activation process, and the presence of several mineral phases including quartz, mullite, gehlenite, anorthite, anhydrite, hematite, and magnesioferrite (Fig. 1). The presence of alumosilicates was also shown through chemical analysis, which proved over 44% of SiO_2 and almost 33% of Al_2O_3 (Table 2) [44]. The main crystalline phase confirmed in the second precursor (metakaolin, MK) was quartz (Fig. 1) with almost 60% being an amorphous phase. In the case of MK, the quantities of SiO_2 and Al_2O_3 were even higher (68 and 25%, respectively), meaning that both precursors exhibit good suitability for alkali-activation. The FTIR spectrum of each precursor is shown in Fig. 2 and reveals that the major band corresponding to the asymmetric stretching vibration of the Si–O–Si and Si–O–Al bonds lies at 988 and 1057 cm^{-1} for FA and MK, respectively. In the MK spectrum, three minor peaks at 797, 780, and 690 cm^{-1} are also present. The peaks near 800 cm^{-1} could be attributed to the O–Al–O bending vibrations of AlO_4 tetrahedra [45]. The difference between the two precursors is also evident from the scanning electron microscopy (SEM) analysis (Fig. 3). In the case of FA, the particles are generally spherically shaped with a diameter ranging from below 1 μm up to 20 μm (Fig. 3a), whereas the MK exhibits finer plate-like particles ranging from below 100 nm up to about 1 μm (Fig. 3b).

2.3. Preparation of the AAFs

Following analysis of the source material, 8 different AAF samples were prepared consisting of varying fly-ash/metakaolin ratios and using different types (sodium- or potassium-based) of activator, as detailed in Table 3. The development of different fly-ash alkali-activated dense materials and corresponding foams has been described in previous studies, from which the optimal two mixtures (1Na and 1K) were adopted in the present paper for further development [44,46]. All lightweight AAFs were therefore foamed with 1 mass % of H_2O_2 and pores were stabilized with the addition of 1 mass % of sodium dodecyl sulfate (SDS) as a surfactant. The fresh foamed pastes were poured into $20 \times 20 \times 80$ mm^3 moulds and cured at 70 °C for 3 days. After 3 days of curing the mechanical strengths were determined (Table S1 and Figs. 5 and 6, samples designated as R.T.). The hardened AAFs were then exposed to elevated temperatures (600, 800, 1000 and 1200 °C) in order to study their dimensional stability, thermal resistance properties as well as their mechanical and microstructural properties after the heat treatment.

2.4. Characterization methods

The chemical composition of the precursors was determined using a

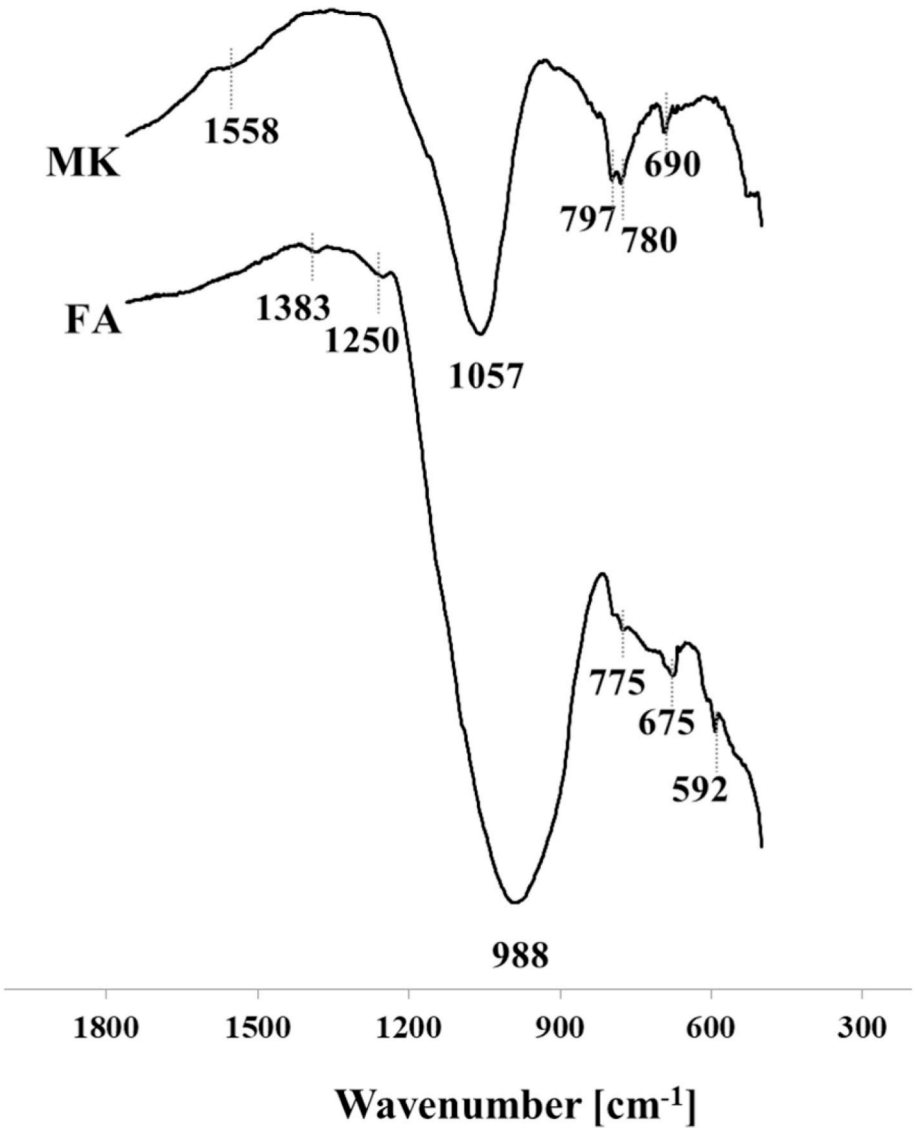

Fig. 2. FTIR spectra of fly-ash (FA) and metakaolin (MK).

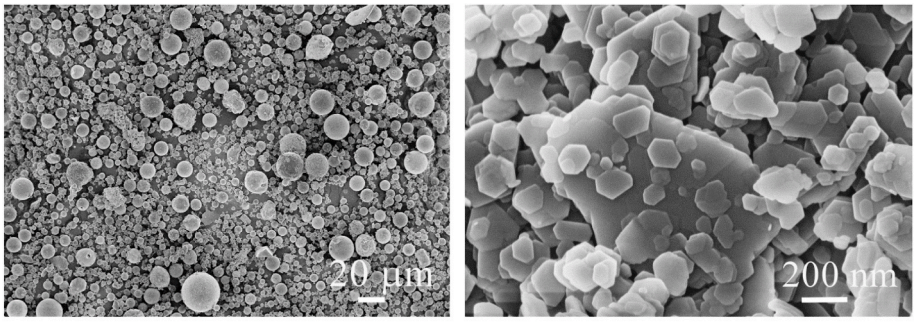

Fig. 3. Scanning electron microscopy (SEM) images of a) FA and b) MK.

Wavelength Dispersive X-ray Fluorescence (WD XRF) analyzer (Thermo Scientific ARL Perform X). The loss on ignition (LOI) of the precursors was determined by the standard method [47].

The mechanical strength (compressive strength) was determined after three days using Toninorm equipment (Toni Technik, Germany; force application rate of 0.05 kN/s) by the standard method [48]. The reported strength measurement values represent the average results obtained from four test specimens of dimensions (20 × 20 × 80) mm^3.

The density of all AAFs was determined by weighing the individual foams and dividing the thus determined weights by the corresponding dimensions of the specimens (i.e. the so called geometrical density).

XRD analysis was determined using a PANalytical Empyrean X ray

Table 3
List of compositions of the different AAFs prepared for the study (all in mass %).

Sample designation	FA	MK	Na_2SiO_3	K_2SiO_3	NaOH	KOH	H_2O_2	SDS	% H_2O
1Na	69.0	/	23.5	/	5.5	/	1.0	1.0	16.0
2Na	51.7	17.3							
3Na	43.0	26.0							
4Na	34.5	34.5							
1K	66.9	/	/	28.9	/	2.1	1.0	1.0	16.7
2K	50.2	16.7							
3K	41.8	25.1							
4K	33.5	33.5							

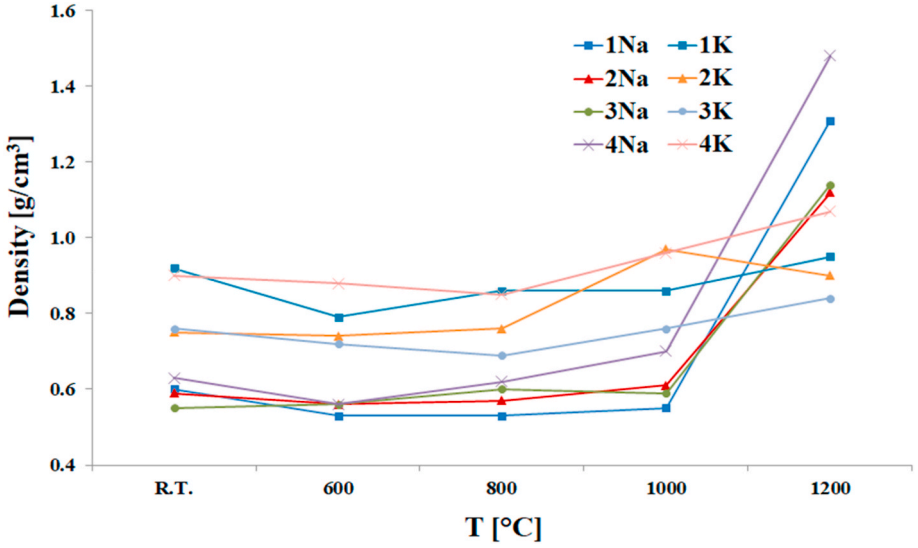

Fig. 4. Graphical representation of the density of each specimen.

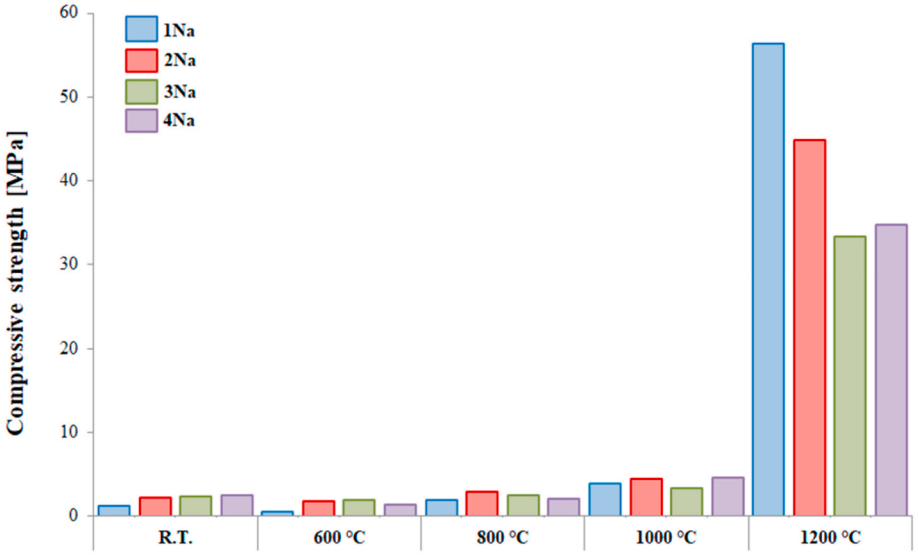

Fig. 5. Graphical representation of the compressive strength of sodium-based specimens before and after exposure to high temperatures (R.T. = room temperature or no exposure).

diffractometer with CuKα radiation (λ = 1.54 Å) at a voltage of 45 kV and a current of 40 mA, in the 2θ range from 5° to 80° (scan rate = 0.026°/min). Data was then analysed with X'Pert High Score Plus diffraction software (PANalytical), using the database PDF 4 + 2015 RDB powder diffraction files. For the amorphous phase determination Rietveld refinement was performed by X'Pert High Score Plus diffraction software, using Al_2O_3 as an external standard.

Dilatometric analysis was performed using a Dilatometer Netzsch DIL 402 up to 1000 °C at a heating rate of 5°/min.

The AAFs investigated were subjected to thermal exposure using a Protherm furnace fired to 600, 800, 1000 and 1200 °C at a heating rate of 600 °C/h and dwelling time of 20 min at any selected temperature.

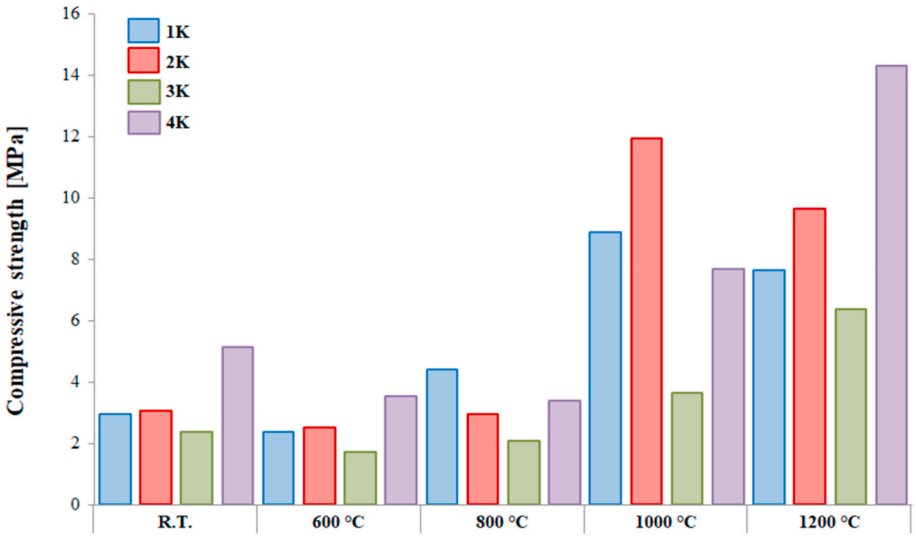

Fig. 6. Graphical representation of the compressive strength of potassium-based specimens before and after exposure to high temperatures (R.T. = room temperature or no exposure).

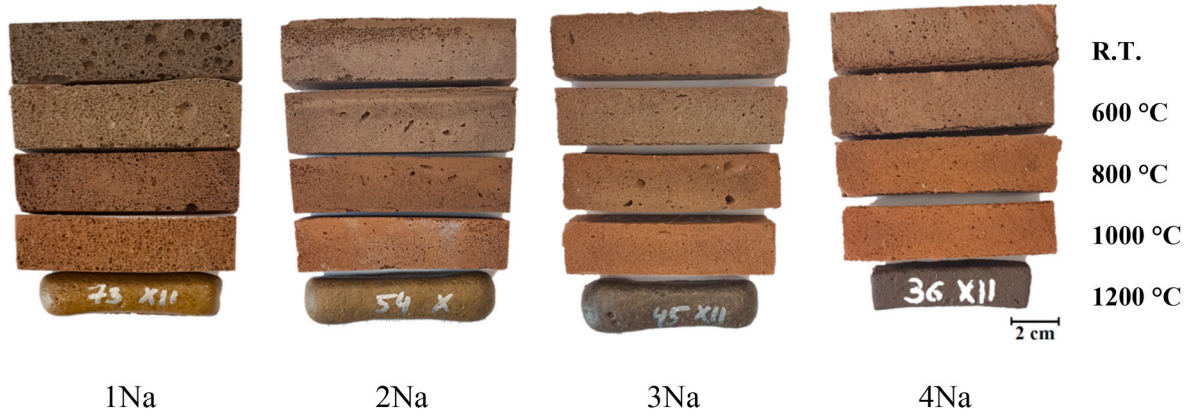

Fig. 7. Macro-images of Na-based samples – unexposed (R.T.) and exposed to elevated temperatures (600, 800, 1000 and 1200 °C).

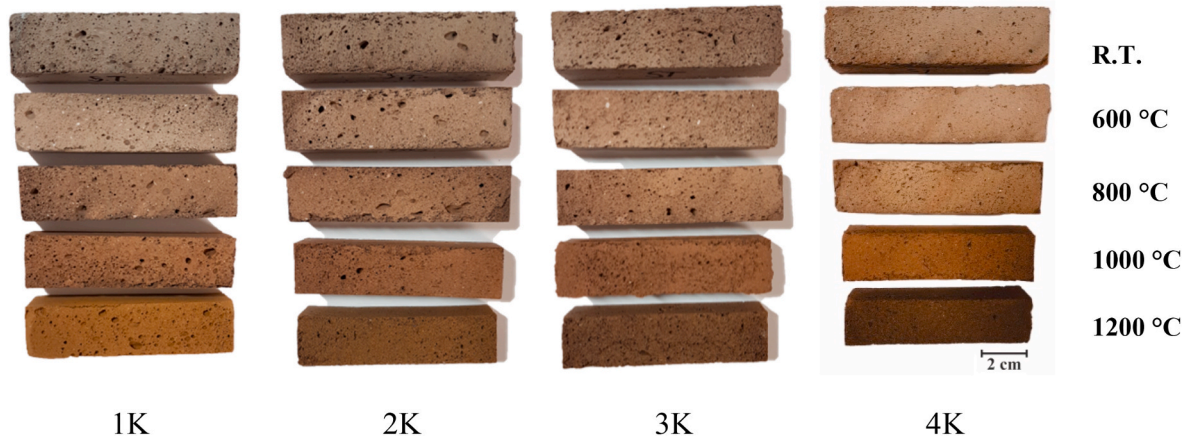

Fig. 8. Macro-images of K-based samples – unexposed (R.T.) and exposed to elevated temperatures (600, 800, 1000 and 1200 °C).

The thermal behaviour of the cured samples was determined by TGA and DTA using a Netzsch Jupiter 449 simultaneous thermal analysis instrument coupled with a mass spectrometer (LC/MS) (Netzsch QMS 403 C Aëolos quadrupole). The analysis was performed in air from 38 to 1100 °C at a heating rate of 10 °C/min using an Al_2O_3 crucible with a lid. The evolution of H_2O and CO_2 were monitored by m/z fragments of 18 and 44, respectively.

Infrared spectra of the hardened AAFs (unexposed and exposed to elevated temperatures) were recorded using a PerkinElmer Spectrum Two FTIR spectrometer equipped with diamond/ZnSe crystal-

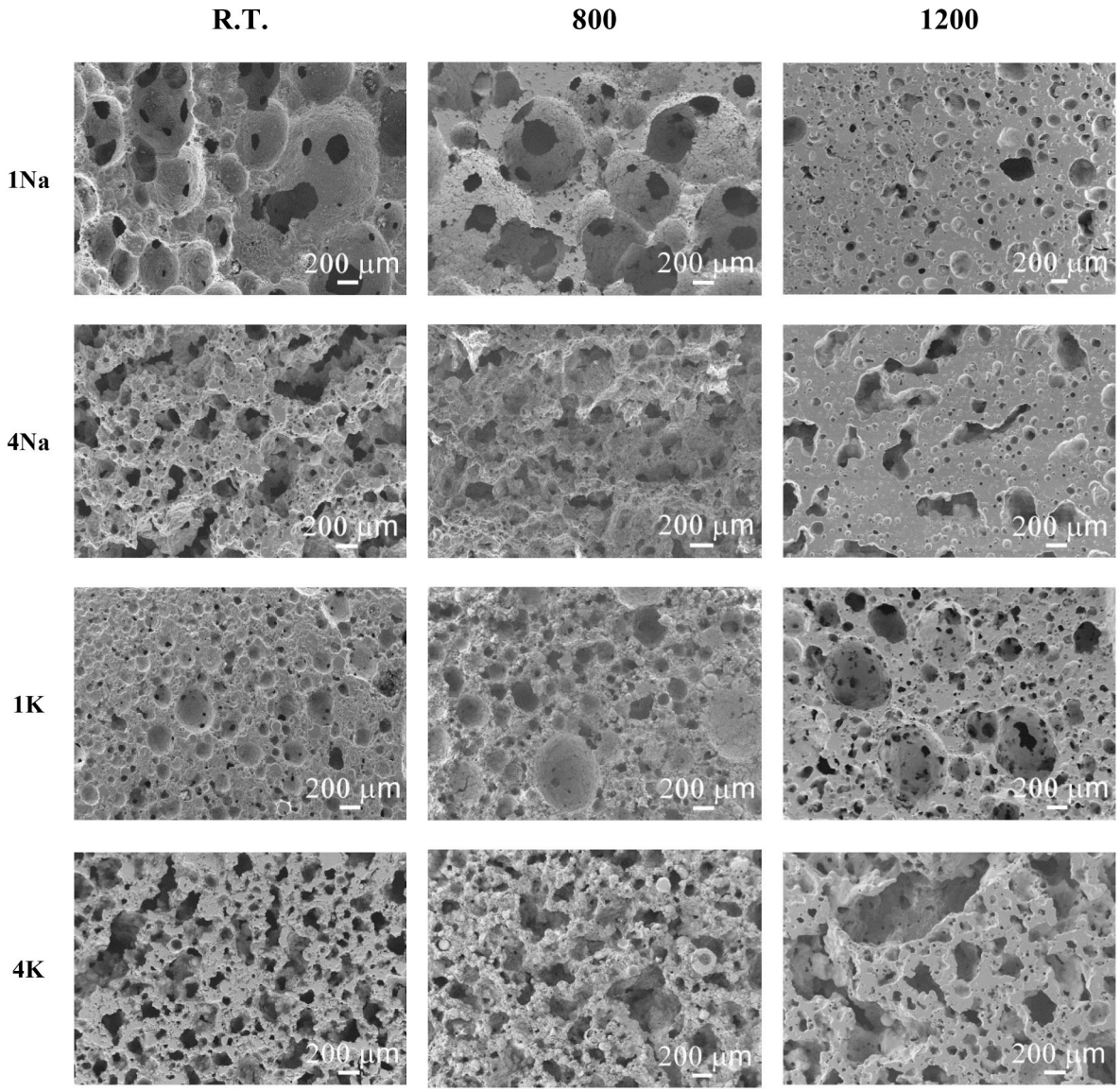

Fig. 9. SEM micrographs at magnification of 120× of selected AAFs before and after exposure to high temperatures.

attenuated total reflection (Universal ATR) as a solid sample support in the range 450–4000 cm^{-1} and a resolution of 1 cm^{-1}. The hardened AAFs were ground prior to analysis.

Microstructural analysis of the precursor and the cross-sections of the hardened and polished AAFs was performed by an Ultra plus FESEM (Carl Zeiss, Germany), with secondary electrons image mode in a high vacuum with the acceleration voltage of 5 kV, magnification of 120× and working distance 5 mm. Prior to SEM scanning, the samples were vacuum-dried and sputter-coated with a 5 nm thick layer of gold.

Figs. 7 and 8 were taken before and after the high-temperature exposure with Cannon SX620 HS and processed with CorelDRAW X8 program.

3. Results and discussions

3.1. Mechanical properties of the hardened AAFs

Graphical presentations of the absolute densities are shown on Fig. 4 and compressive strengths on Figs. 5 and 6. Additionally, the absolute and relative mechanical properties and densities of the unexposed (designated as R.T.) and fired samples are given in Table S1. In a system activated by sodium activators, it can be observed that the compressive strength of the unexposed samples ranges between 1.24 and 2.55 MPa and the density between 0.55 and 0.63 g/cm^3. The higher values of compressive strength are, however, attributed to the greater addition of metakaolin to the mixture. The addition of metakaolin has therefore contributed to the compressive strength gain in samples 2Na, 3Na and 4Na - 75, 84 and 106% respectively - which is in line with the increased quantity of metakaolin (respectively 17, 25 and 33 mass %) added to the mixture. After exposure to 600 °C there is a drop in the compressive strength of all samples (to 45, 85, 86 and 53% for samples 1Na, 2Na, 3Na and 4Na, respectively). The drop in compressive strength is greater with a bigger decrease in density (an 88% decrease in density resulted in strength losses of 46 and 53% for specimens 1Na and 4Na, respectively). In our case, it is probably the consequence of several influencing factors. After firing up to 1000 °C the compressive strength of all specimens increases (from 143 to 300%), even though the densities change by a maximum of 10%. This could also be explained by the occurrence of the new crystalline phase (nepheline, Figs. 13 and 14). When fired up to 1200 °C a significant increase in density is observed in all samples (max. 235% for specimen 4Na) as a result of the vitrification process and consequently accompanied by a notable increase in compressive strength (compressive strength is 45 times greater in specimen 1Na). Even though the sample with the highest amount of metakaolin added

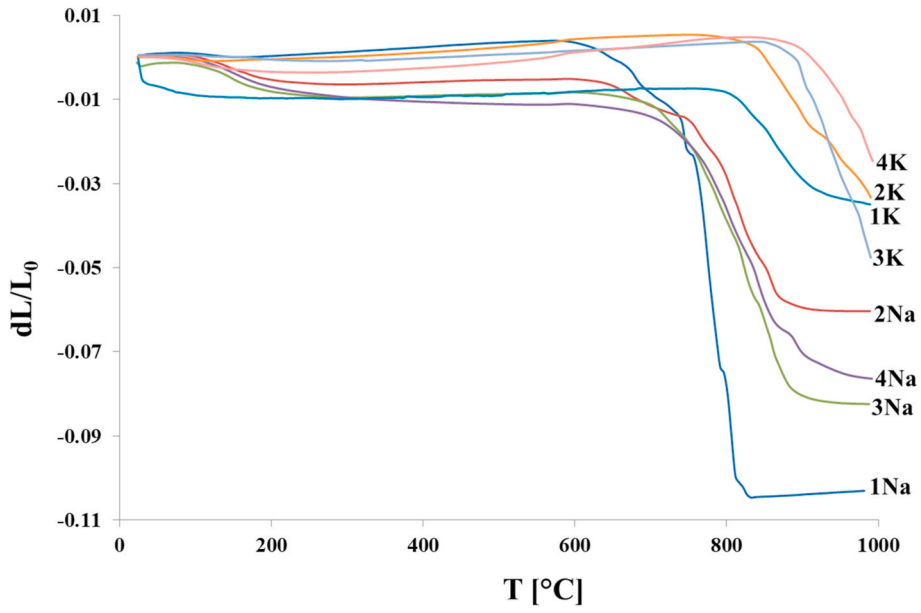

Fig. 10. Thermal deformation characteristics of AAFs observed using a dilatometer.

(specimen 4Na) gained the highest density, the lowest compressive strength at that temperature was exhibited at the same time, confirming the thesis proposed by Kong et al. [15]. They concluded that metakaolin-based alkali-activated materials are more fragile than fly-ash based systems when exposed to elevated temperatures.

In the system with potassium activators, compressive strengths are higher than in the sodium-based system, ranging between 2.94 and 5.12 MPa. This is partly as a result of the generally higher densities, namely 0.92, 0.75, 0.76 and 0.90 g/cm^3 for specimens 1K, 2K, 3K and 4K, respectively (Fig. 4). Again an increment in compressive strength is noticed in line with the increased addition of metakaolin (except in the case of the 3K sample). After firing to 600 °C a decrease in compressive strength (resulting in between 69 and 82% of initial strength) is also observed for all the potassium-based samples, most probably for the same reason as in the case of the sodium-based samples. Further firing similarly contributed to sample densification, an improvement in mechanical properties, and new crystalline phases that could contribute to the increase in strength are also observed here (Figs. 14 and 15). Contrary to the sodium-based system, in the case of the potassium-based system, the highest compressive strength after exposure to 1200 °C was measured in the 4 k specimen, to which the highest amount of metakaolin had been added. Potassium-based samples, however, generally exhibit lower densities (Fig. 4) and thus lesser mechanical properties at that temperature compared to sodium-based specimens, due to improved resistance to high temperatures and their less sinterable nature, as demonstrated later in the paper.

3.2. Microstructural analysis

The sodium- and potassium-based AAFs before and after exposure to elevated temperatures are shown in Figs. 7 and 8. The change in colour from greyish to brownish is observed for both types of sample after exposure to temperatures of 800 °C and above [43]. It is also evident that shrinkage is greatest in the case of sodium-based samples exposed to 1200 °C, where the consequences of the vitrification process on the material are also visible.

To provide further insight into the structure of the AAFs, SEM was utilised to attain cross-sectional micrographs of the selected boundary specimens before and after exposure to elevated temperatures (Fig. 9). Before exposure to an elevated temperature, the fly-ash based samples (1Na and 1K) have a porous microstructure with clearly developed circular pores, which are evenly distributed and connected to one other. Contrarily, the addition of fine metakaolin (4Na and 4K) to the mixture affects the pore structure, making them become more disordered. They exhibit high structural heterogeneity whilst containing hardly any rounded pores. In both cases, however, numerous unreacted fly-ash particles integrated within the AAM skeleton are also observed. The micrographs of specimens exposed to 800 °C reveal no significant differences compared to those of specimens before exposure. Contrarily, after exposure to 1200 °C, a transformation in the microstructure is evident in both sample types as a result of the vitrification process. The sodium-based AAFs, however, look more compact (more dense) with fewer pores, as supported by the density measurements (sodium-based AAFs are denser than potassium-based AAFs; see Table S1). Viscous sintering is responsible for the collapse of nano-pores, stronger inter-particle bonding, healing micro-cracks and densification of the matrix [10,15], as also observed in this study. Potassium-based AAFs, on the other hand, showed less of a “denser texture” compared to sodium-based AAFs, since potassium-based AAFs are more resilient to densification due to an increased strength of Al–O bonds in the presence of potassium compared to sodium [49]. Furthermore, it is also generally known that, because they are bigger, potassium cations have significantly lower diffusivity than sodium cations. Materials containing potassium therefore exhibit a less sinterable nature than identical materials containing sodium.

3.3. Dilatometry analysis

Materials tend to expand or shrink when subjected to elevated temperatures; therefore the thermal deformation characteristics of alkali-activated materials are of particular importance when evaluating their potential for high temperature applications. This can be measured ex-situ through dimensional measurements or in-situ using techniques such as dilatometry. Dilatometry is a traditional method used to precisely measure dimensional changes of a material as a function of temperature [50].

Generally examining the thermal deformation shown in Fig. 10, it can be noted that the thermal deformation characteristics of the specimens studied could be divided into four notable temperature regions with regard to the extent of deformation. In the first region (25–200 °C) small dimensional changes occur, which could be attributed to the dehydration of free and weakly bound water given that samples were

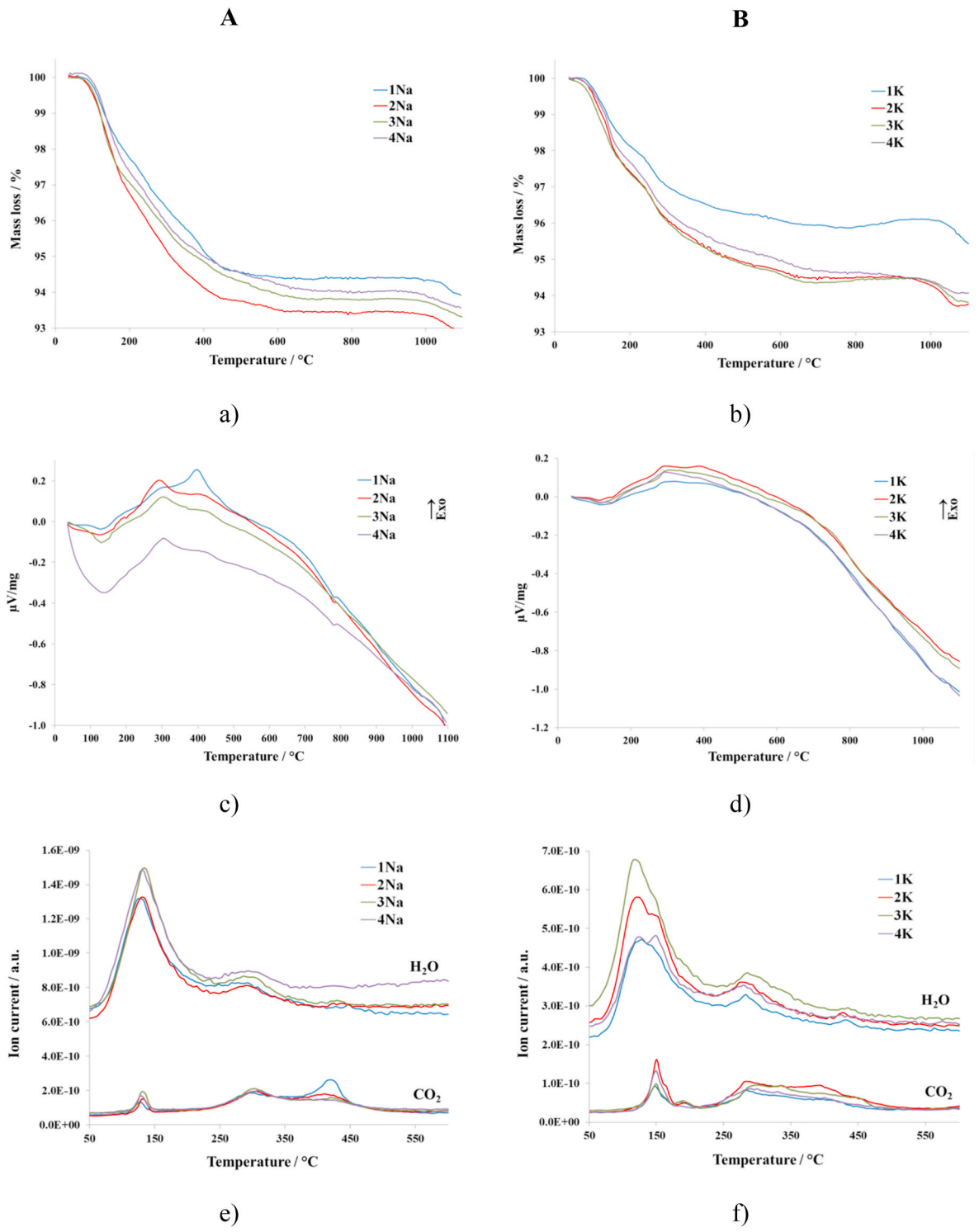

Fig. 11. Thermogravimetric and differential thermal analysis (TG-DTA) coupled with mass-spectrometry (MS) of sodium-based (**A**) and potassium-based (**B**) AAFs (mass loss: a) and b); heat flow: c) and d); ion current signal relative to water and carbon dioxide: e) and f)).

not dried in an oven before the dilatometry test. The shrinkage in this region is most obvious in the case of the 1K specimen and also observed in all the sodium-based AAFs. The second region, between 200 °C and 600 °C, is similar for all eight specimens with only minor changes in dimension being observed. The third and fourth regions vary between sodium and potassium-based foams. For sodium-based AAFs the third region occurs between 600 and approximately 850 °C and consists of remarkable shrinkage corresponding to the glass transition temperature. The reaction products and the pore structure of the samples collapse at the glass transition temperature, at which point the Si–O–Al framework softens and a sintering process takes place [51,52]. At temperatures above 850 °C (the fourth region) again only small dimensional changes are observed. The third region for potassium-based AAFs is between 600 and 800 °C, where a slight expansion of the material is observed, followed by a region above 800 °C, where densification and sintering take place.

The results also show that the least thermal deformation occurred in the case of the 4K specimen, while the 1Na specimen exhibited the most.

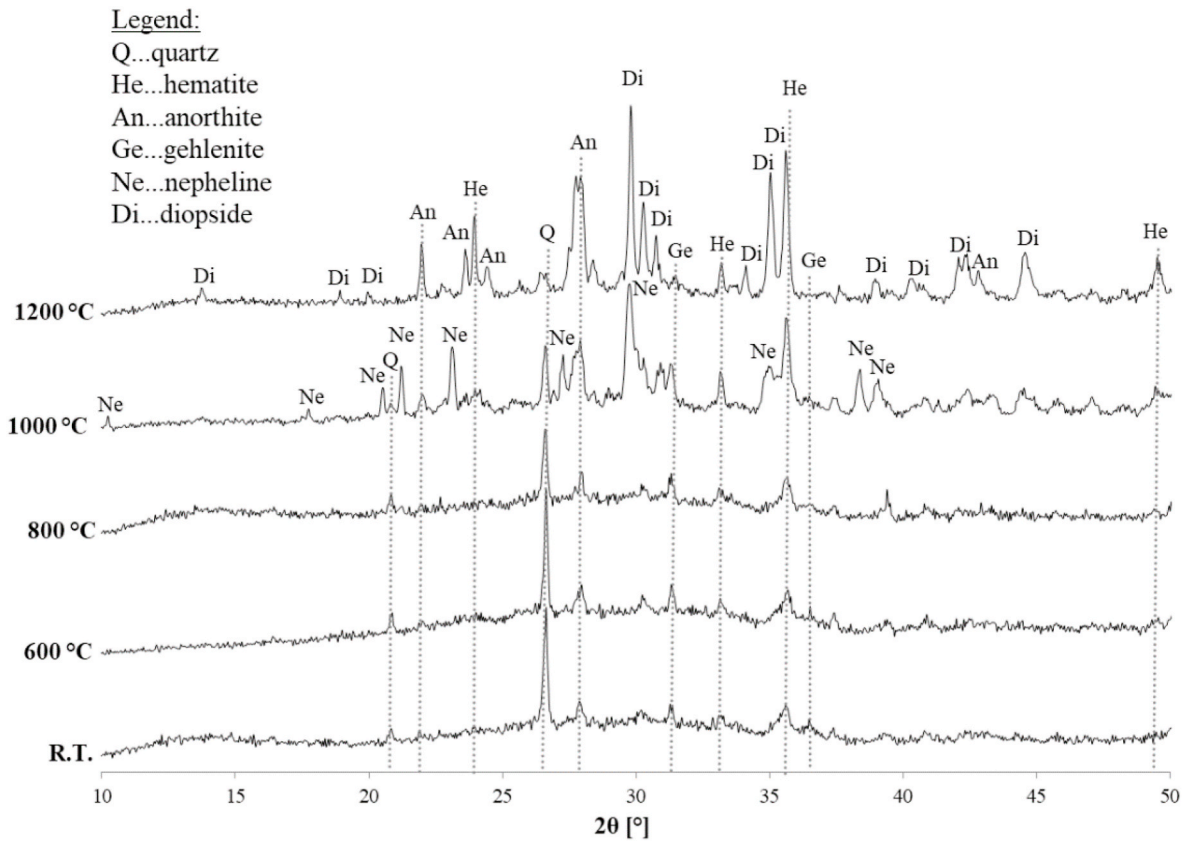

Fig. 12. X-ray diffractograms of sample 1Na exposed to room and elevated temperatures.

Lahoti et al. also concluded that potassium-based foams generally undergo minor thermal deformation in comparison to sodium-based foams [53]. It could also be concluded that the addition of metakaolin enhances the material's resistance to high temperatures since almost all the specimens containing metakaolin (except specimen 3K) underwent lower thermal shrinkage than specimens containing only fly-ash (1Na and 1K). The positive effect of adding metakaolin to the AAFs is further reflected by the temperature at which the material starts to significantly shrink (sinter). Sodium-based AAFs without metakaolin start to shrink at about 600 °C (1Na), whereas specimens with metakaolin added do not start to shrink until about 700 °C. A similar trend is also observed in the potassium-based AAFs, where the 1K specimen starts to shrink at about 800 °C while specimens containing metakaolin don't start to shrink until about 900 °C. Overall it could be concluded that both the type of cation, as well as the addition of metakaolin, can greatly affect the materials' resistance properties to high temperature. By selecting appropriate precursors and activators, shrinking commenced at a 300 °C higher temperature, and total shrinkage was reduced by 7%. Further, potassium as cation type seems to have double role from the point of view of the mechanism. Firstly, it prevent sample from higher shrinkage since it is bigger cation in comparison to sodium [54]. And secondly, together with the metakaolin addition, it influences the Si/Al/K ratio in the final composition to be more close to the leucite composition, and thus improving refractory properties by forming thereof at elevated temperatures. Leucite phase transition and thermal expansion has already been studied in details elsewhere [55] and authors concluded that both parameters were found to be highly tailorable by controlling alkali cation stoichiometry. To add, higher Si/Al ratio, which was in our case attained by the metakaolin addition (content of the SiO_2 in the FA and MK is 44.8 and 68.1, respectively, as seen from Table 2) has already been recognised as a strong influencing parameter on the behaviour of AAMs at high temperatures. The extent of crystallization decreases with the increasing Si/Al ratio (t.i. the amount of amorphous content that crystallises). Directly connected to that is the onset temperature of the crystallization, which also increases with the Si/Al ratio and in general terms it could be concluded that the higher Si/Al ratio is leading to greater phase stability of the AAMs paste during the high temperature exposure [56,57].

3.4. TG-DTA and MS analysis

The behaviour during thermal treatment was studied by thermal analysis coupled with mass spectrometry. The evolution of mass loss, heat flow, and signal mass m/z 18 (H_2O) and m/z 44 (CO_2) are plotted as a function of temperature from 38 °C to 1100 °C (Fig. 11). No signals other than those related to water and carbon dioxide were detected during the analysis. Comparing the plots for mass loss the first main difference observed is the variation between each sample. After heat treatment at 1000 °C the mass loss of the sodium-based foams (Fig. 11a) was between 5.7 and 6.6%, compared to a variation of 4.0–5.6% in the potassium-based foams (Fig. 11b). Since the water content present in the initial reactive mixture (Table 2) was very similar in both cases (16.0 and 16.7%, respectively), the difference in mass loss could not be associated with the difference in water consumption during the foam formation at 70 °C, as has been reported in other studies [58]. Even though some differences in mass loss exist between samples, on the other hand, there are similarities in the DTA and MS plots. In all samples, we can observe one endothermic peak around 140 °C and two exothermic peaks at around 300 °C and 400 °C. All three peaks are accompanied by the detection of the signal m/z 18, corresponding to H_2O molecules, which shows the loss of water, and of the signal m/z 44, corresponding to CO_2. In inorganic materials, such as alkali-activated materials, water can be found in three main forms: (i) hygroscopic (free) water, which is removed at rising temperatures of up to 120 °C (ii) physically bonded water, removed between 120 and 300 °C [59,60], and (iii) chemically bound water, which starts to be removed when the temperatures exceed

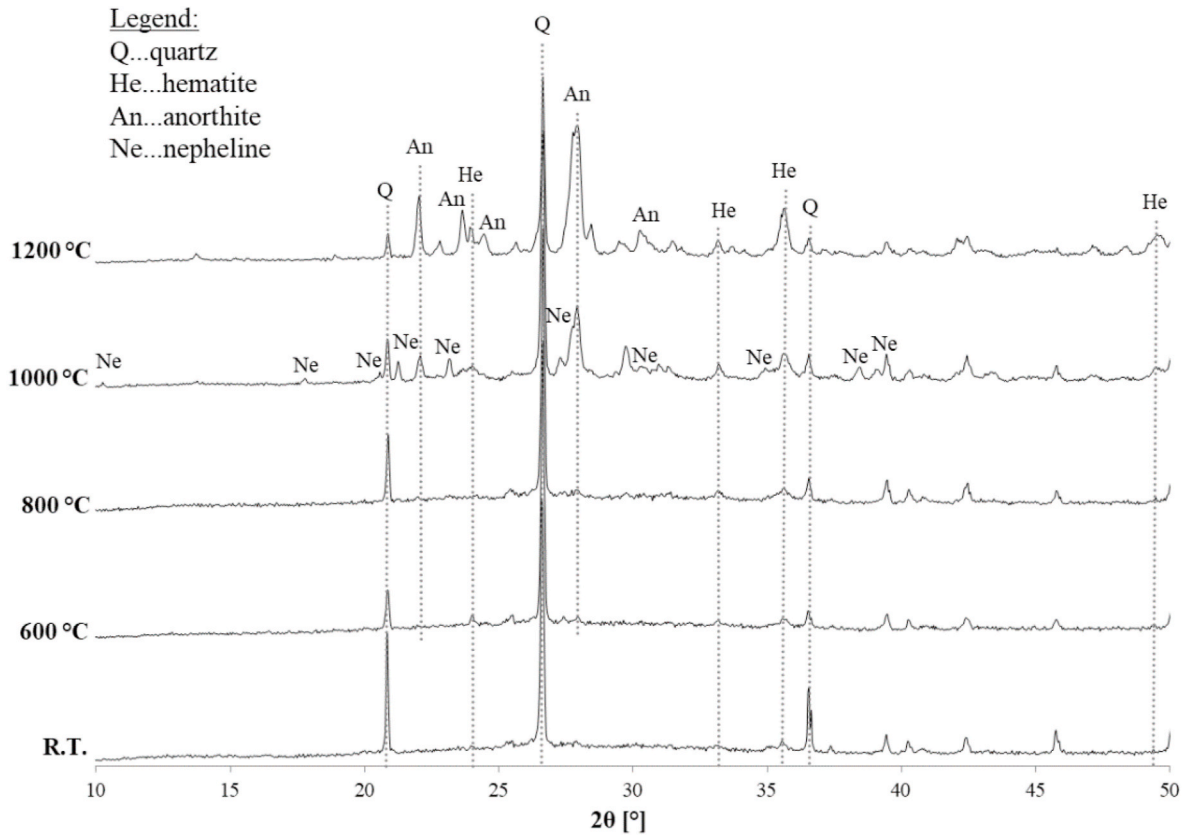

Fig. 13. X-ray diffractograms of sample 4Na exposed to room and elevated temperatures.

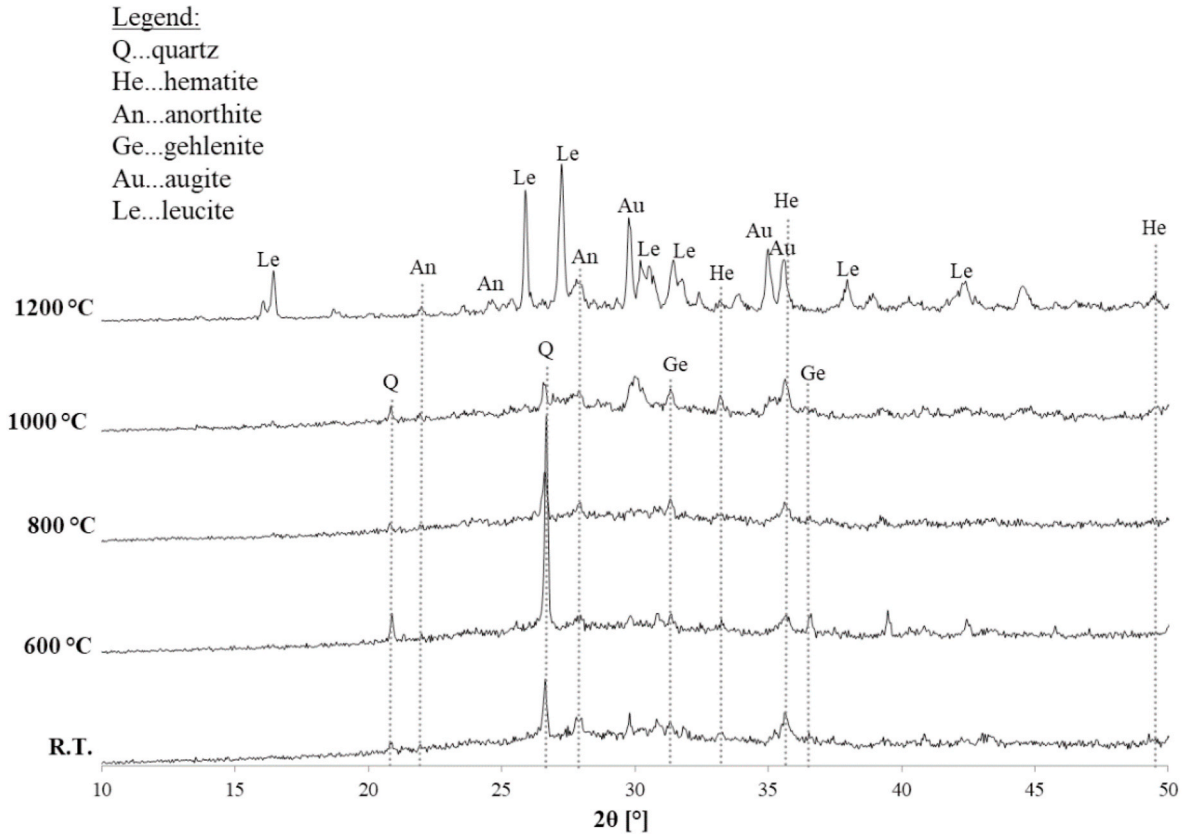

Fig. 14. X-ray diffractograms of sample 1K exposed to room and elevated temperatures.

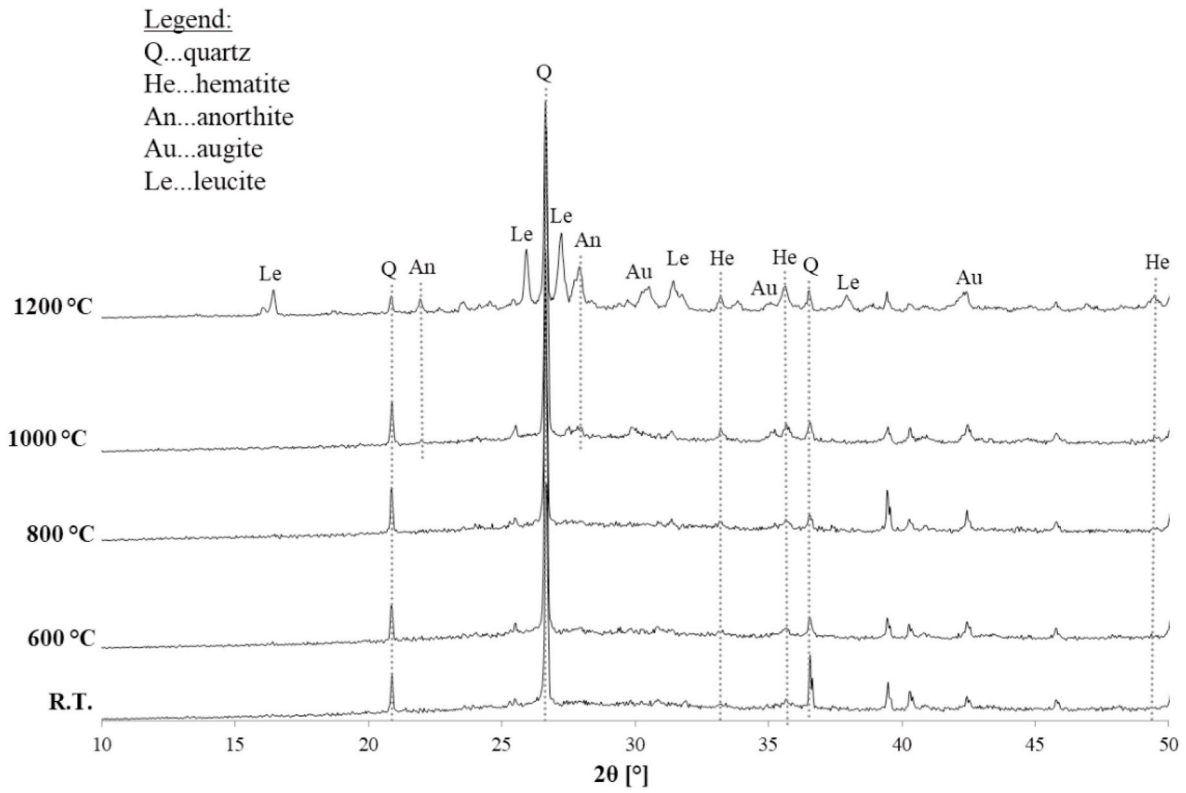

Fig. 15. X-ray diffractograms of the 4K sample exposed to room and elevated temperatures.

300 °C. The first peak in our case could therefore indicate the evaporation of crystallization water and the second one absorbed water in the aluminosilicate gel phase (water from hydrogels). The peaks in the DTA curve correspond to the decomposition of metal and –OH group compounds (acids, basics and neutral compounds such as $Si(OH)_4$, $Fe(OH)_3$, NaOH, KOH, $Al(OH)_3$) [60]. In our case this is the peak at around 400 °C. In the case of sodium-based foams, the DTA curves show a more intense signal, together with a higher number of H_2O molecules on MS spectra, compliant with a greater mass loss as well as greater thermal shrinkage, as shown in Fig. 10. Additionally, the *m/z* 44 signal, corresponding to CO_2, could be attributed to the organic part, which could either have been incorporated into the fresh mix through the addition of a surfactant (sodium dodecyl sulfate - SDS) or was found in the precursor itself (LOI were 0.51 and 2.14% for FA and MK, respectively; see Table 3).

3.5. Mineralogical analysis

Material characterization techniques, namely XRD and FTIR, were used to obtain a better understanding of the possible transformations which could have taken place to lead to the diversity of mechanical properties. Due to a large number of samples, only boundary compositions (1Na, 4Na, 1K, and 4K) will be presented, but similar observations were seen in all specimens studied. Firstly, the results of the XRD analysis of selected specimens before and after exposure to elevated temperatures are shown as stacked plots (Figs. 12–15). The main crystalline phases identified in the precursors, such as quartz and hematite, were also found in the unexposed AAFs. These phases were present in all samples, regardless of the precursor used for the alkali-activation process, whereas anorthite was present only in the AAFs in which fly-ash was used as a precursor. Hematite and anorthite, for example, were barely affected by either the alkali-activation process or exposure to a high temperature (given their melting points of approximately 1565 and 1553 °C, respectively), so they can therefore also be observed in the spectra of specimens exposed to 1200 °C. Moreover, the peak intensity of the hematite phase even increases with an increased temperature, probably due to its recrystallization from the amorphous iron in fly-ash [61]. Quartz, on the other hand, remains stable up to 1200 °C in AAFs where both precursors are present (FA and MK; specimens 4Na and 4K), while in the specimens where only fly-ash was used as the precursor (specimens 1Na and 1K) the peaks for quartz disappeared at 1200 °C. That could be due to the increased presence of free alkalis in the fly-ash based AAFs (where less Si is available for the alkali-activation process), which can dissolute/melt the quartz in the AAM matrix at lower temperatures, since alkalis are known to contribute to the eutectic melting of quartz [60]. A similar decrease in quartz intensity was also observed by He et al. [62], although in their study the dissolution of quartz first appeared at exposure to 1000 °C for 120 min, which is significantly longer than in our case (20 min). Another possible explanation for the decrease in quartz intensity would also be its transformation to tridymite, also observed by Korat and Ducman [43], but in our case, the peaks for tridymite could not be proven without a doubt.

Sodium-based AAFs maintain their thermal stability up to 800 °C, with respect to mineralogical content, since no significant changes are observed in the phase compositions for either specimen (1Na and 4Na). The first major changes are therefore observed at exposure to 1000 °C, where a new phase starts to crystalize into nepheline ($NaAlSiO_4$), as expected and previously found in the literature [63]. The high temperature phase nepheline is also reported to improve the thermal resistance of the alkali-activated materials, due to its high melting point [61]. It can be seen from the XRD pattern that, due to the presence of silicon dioxide, nepheline is no longer stable at 1200 °C therefore feldspars will form which vary according to the amount of calcium available [64]. In both specimens, anorthite ($CaAl_2Si_2O_8$) is formed. In the case of the 1Na specimen, where a higher amount of Ca is available, as well as sufficient Al_2O_3 content, the formation of diopside ($MgCaSi_2O_6$) is also observed [65]. Potassium-based AAFs, on the other hand, maintain higher thermal stability up to 1000 °C. The major changes are therefore observed at 1200 °C, where new phases start to crystalize into leucite ($AlKSi_2O_6$) as

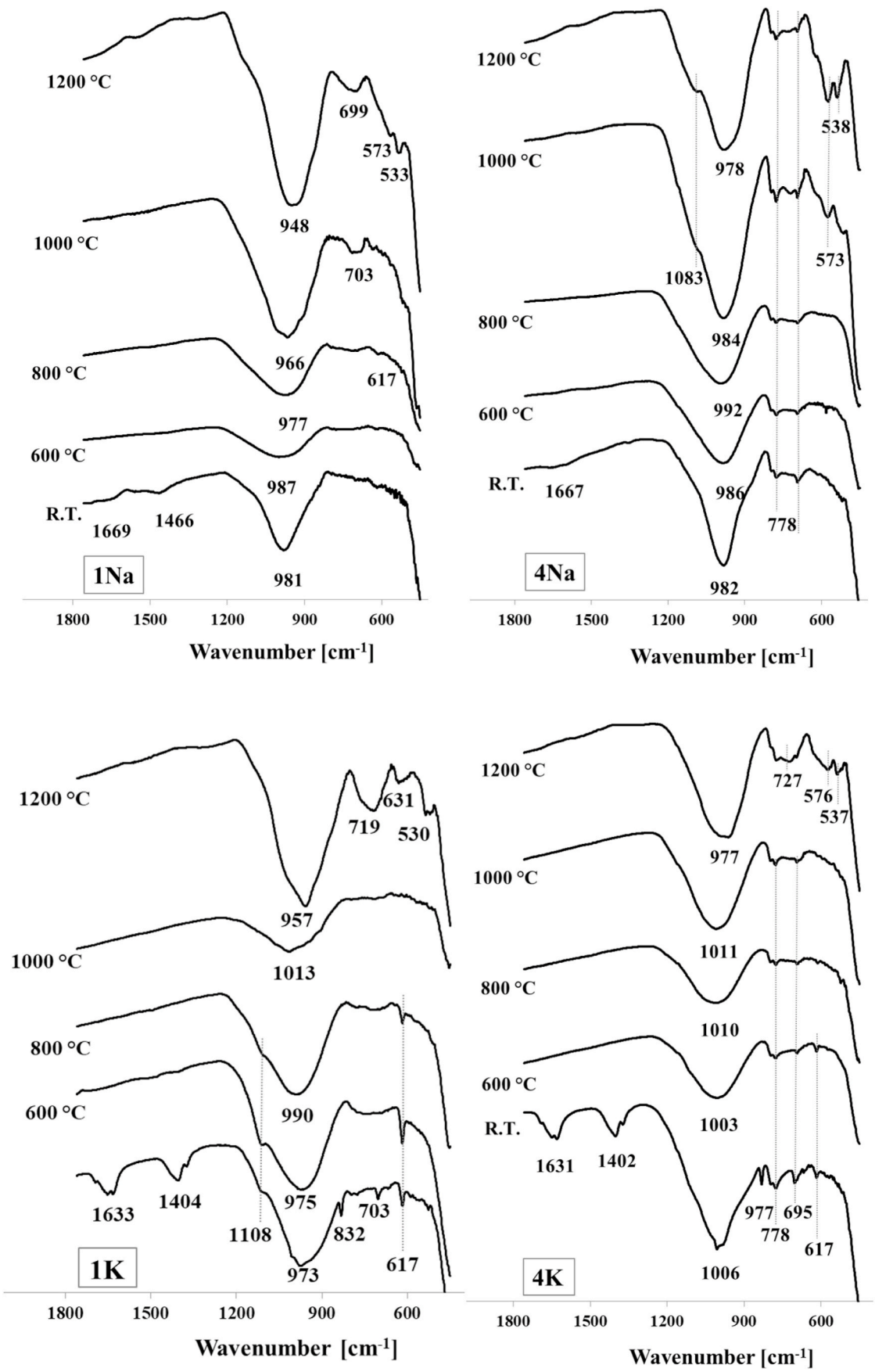

Fig. 16. FTIR spectra of 1Na, 4Na, 1K and 4K specimens exposed to room and elevated temperatures.

the predominant phase (similar findings were found also by Bell et al. [3]) together with anorthite and augite ((Ca,Na) (Mg,Fe,Al,Ti) (Si, Al)$_2$O$_6$).

3.6. FTIR analysis

FTIR analysis was performed in order to confirm the hypothesis that the formation of a crystalline phase will induce modification of the network and therefore also modify the bond vibrations in materials, as reflected by changes in the IR spectra [66]. Fig. 16 shows the FTIR spectra of the original alkali-activated matrix before (denoted as R.T.) and after exposure to elevated temperatures for selected boundary specimens (1Na, 4Na, 1K, and 4K). It can be noted that the main band for asymmetric stretching of the T–O–T bond (where T is Si or Al) in all four spectra of selected alkali-activated foams is 981, 982, 973, and 1006 cm^{-1} for 1Na, 4Na, 1K and 4K, respectively, and that it is different to the main band observed in the spectra of the initial precursors (see Fig. 2; 1057 and 988 for MK and FA, respectively). Similar shifts have been observed previously by Lahoti et al. [33]. In three of the selected AAFs, due to exposure to 600 °C, the main asymmetric stretching band showed only slight broadening and a minor shift in the peak position, suggesting chemical stability that is also consistent with the XRD observations. The broadening of the main bond band, however, was observed due to the structural disorder caused by the heating of the material. It can also be observed that the broadening of the band is not as obvious in potassium-based AAFs compared to sodium-based foams, as was also observed by Lahoti et al. [53]. This is because sodium-based AAFs experienced higher structural disorder caused by evaporation of physically bonded water, together with the sintering process (also shown in sections 3.3 and 3.7), whereas the sintering process in potassium-based AAFs takes place at much higher temperatures. Contrarily, after exposure to 800 °C, the difference in the position of the main peak is more noticeable, even though no new crystalline phases are observed in the XRD spectra of selected specimens at that temperature. The change in the IR spectra could therefore be a consequence of a change in the amorphous phase of a matrix. The biggest shift in the main band peak (948, 978, 957, and 977 cm^{-1} for 1Na, 4Na, 1K, and 4K, respectively) is observed after exposure to 1200 °C, indicating bigger changes in the alkali-activated network as well as the occurrence of new crystalline phases. The presence of a shoulder around 1100 cm^{-1} can be noted on some spectra (4Na and 1K) and is attributed to a Si–O–Si bond in amorphous silica, indicating a residual presence of the precursor [58]. The bands around 770 and 550 cm^{-1} could also be attributed to the presence of Si–O–Si and O–Si–O bonds in various configurations, constituting part of the foam network [66]. With the occurrence of new phases at 1000 and 1200 °C, new peaks are also observed in the IR spectra in the region between 500 and 800 cm^{-1}. In the literature, the formation of nepheline has been indicated by the appearance of peaks around 450 cm^{-1} and 690 cm^{-1}, and a shoulder at 1080 cm^{-1}, as could also be argued in our case for the 1Na and 4Na specimens [33].

Interesting phenomena are observed in the region between 1400 and 1650 cm^{-1}, where two weak bands are observed in all specimens before heat treatment (only in the spectra of the 4Na specimen the peak at around 1400 cm^{-1} is not observed, probably due to the poor signal to noise ratio). The first band at approximately 1650 cm^{-1} is attributed to the H–O–H bending vibrations in the water and the second, at approximately 1400 cm^{-1}, to the vibrating modes of the CO_3^{2-} contained in $CaCO_3$. Both peaks in the IR spectra of specimens disappear when treated at 600 °C (and higher), suggesting that water and CO_2 are released during the heat treatment, as was also proven by the TG-DTA coupled with MS analysis (Fig. 11).

4. Conclusions

In order to improve the thermal stability of alkali-activated foams, fly-ash based foams have been optimized by adding metakaolin, and changing the activator from sodium-based components to potassium-based components. The following conclusions can be drawn:

- The addition of metakaolin, as well as a change in activator type, has a significant impact on the mechanical properties of the foams. In both systems, the mechanical strength increases when the amount of metakaolin added to the mixture is increased (with one exception – specimen 3K). Generally, better mechanical strength is achieved in the potassium-based systems (also due to the higher densities), except when samples are exposed to 1200 °C at which point the better properties of resistance to high temperature and less sinterable nature of the potassium-based samples take priority.
- Samples containing only fly-ash content (1Na and 1K) have a porous microstructure with round pores, which becomes more distorted with the addition of metakaolin. In both sample types, a transformation in the microstructure is evident after exposure to 1200 °C, due to the vitrification process – the structure looks more compact (smoother) with fewer pores.
- The addition of metakaolin and change of activator to potassium-based components caused an overall increase in the thermal resistance of approximately 300 °C (thermal stability from 600 °C for sodium-based fly-ash foams, to 900 °C for potassium-based fly-ash foams with the addition of metakaolin).
- Microstructural evaluation by XRD revealed the occurrence of nepheline as a new crystalline phase at 1000 °C in the case of the sodium-based foams, whereas potassium-based foams showed higher thermal stability and thus the occurrence of new phases only at 1200 °C (leucite as the predominant phase together with anorthite and augite). FTIR analysis, on the other hand, revealed that the significant difference of the main peak position is observed once exposed to 800 °C, meaning that a change in the amorphous phase of a matrix starts even before the occurrence of new phases.

The present results confirmed that the properties of such foams make them suitable for potential applications up to 800 °C, potentially replacing competitive materials which are being produced by less environmentally-favourable processes. Namely, the main benefits of AAFs are their utilization of waste and the application of a low temperature process, which together lowers the production costs, saves virgin raw materials, and lowers the carbon footprint.

Declaration of competing interest

The authors declare that they have no known competing financial interests or personal relationships that could have appeared to influence the work reported in this paper.

Acknowledgements

The authors would like to thank the Slovenian Research Agency (ARRS) for the project grant J2 9197: “Synthesis and characterization of alkali activated foams based on different waste”.

Appendix A. Supplementary data

Supplementary data to this article can be found online at https://doi.org/10.1016/j.ceramint.2021.05.241.

References

[1] R. Pierrehumbert, There Is No Plan B for Dealing with the Climate Crisis, Bulletin of the Atomic Scientists, 2019, pp. 1–7.
[2] R.M. Andrew, Global CO2 emissions from cement production, Earth Syst. Sci. Data 10 (2018) 195–217, https://doi.org/10.5194/essd-10-195-2018.
[3] J.L. Bell, P.E. Driemeyer, W.M. Kriven, formation of ceramics from metakaolin-based geopolymers. Part II: K-based geopolymer, J. Am. Ceram. Soc. 92 (3) (Mar 2009) 607–615, https://doi.org/10.1111/j.1551-2916.2008.02922.x.

[4] J.L. Provis, J.S.J. van Deventer (Eds.), Alkali Activated Materials: State-Of-The-Art Report, RILEM TC 224-AAM, (State-Of-The-Art Report, RILEM TC 224-AAM), Springer/RILEM, Berlin, 2013.

[5] T. Luukkonen, Z. Abdollahnejad, J. Yliniemi, P. Kinnunen, M. Illikainen, One-part alkali-activated materials: a review, Cement Concr. Res. 103 (2018) 21–34, https://doi.org/10.1016/j.cemconres.2017.10.001.

[6] B. Horvat, V. Ducman, Potential of green ceramics waste for alkali activated foams, Materials 12 (21) (Nov 2019), https://doi.org/10.3390/ma12213563. Art no. 3563.

[7] A. Alzaza, et al., Production of lightweight Alkali activated mortars using mineral wools, Materials 12 (10) (May 2019), https://doi.org/10.3390/ma12101695. Art no. 1695.

[8] J.L. Provis, Alkali-activation of calcined clays - past, present and future, in: F. Martirena, A. Favier, K. Scrivener (Eds.), Calcined Clays for Sustainable Concrete vol. 16, RILEM Bookseries, 2018, pp. 372–376.

[9] Ferone Messina, Roviello Colangelo, Cioffi, Alkali activated waste fly ash as sustainable composite: influence of curing and pozzolanic admixtures on the early-age physico-mechanical properties and residual strength after exposure at elevated temperature, Compos. B Eng. 132 (Jan 2018) 161–169, https://doi.org/10.1016/j.compositesb.2017.08.012.

[10] P. Duxson, G.C. Lukey, J.S.J. van Deventer, Thermal evolution of metakaolin geopolymers: Part 1 - physical evolution, J. Non-Cryst. Solids 352 (52–54) (Dec 2006) 5541–5555, https://doi.org/10.1016/j.jnoncrysol.2006.09.019.

[11] J.L. Provis, Alkali-activated materials, Cement Concr. Res. 114 (2018) 40–48.

[12] A.M. Rashad, S.R. Zeedan, The effect of activator concentration on the residual strength of alkali-activated fly ash pastes subjected to thermal load, Construct. Build. Mater. 25 (7) (Jul 2011) 3098–3107, https://doi.org/10.1016/j.conbuildmat.2010.12.044.

[13] K. Traven, M. Češnovar, V. Ducman, Particle size manipulation as an influential parameter in the development of mechanical properties in electric arc furnace slag-based AAM, Ceram. Int. 45 (17) (Dec 2019) 22632–22641, https://doi.org/10.1016/j.ceramint.2019.07.296.

[14] S.A. Bernal, E.D. Rodriguez, R.M. de Gutierrez, M. Gordillo, J.L. Provis, Mechanical and thermal characterisation of geopolymers based on silicate-activated metakaolin/slag blends, J. Mater. Sci. 46 (16) (Aug 2011) 5477–5486, https://doi.org/10.1007/s10853-011-5490-z.

[15] D.L. Kong, J.G. Sanjayan, K. Sagoe-Crentsil, Comparative performance of geopolymers made with metakaolin and fly ash after exposure to elevated temperatures, Cement Concr. Res. 37 (12) (Dec 2007) 1583–1589, https://doi.org/10.1016/j.cemconres.2007.08.021.

[16] T.A. Aiken, W. Sha, J. Kwasny, M.N. Soutsos, Resistance of geopolymer and Portland cement based systems to silage effluent attack, Cement Concr. Res. 92 (Feb 2017) 56–65, https://doi.org/10.1016/j.cemconres.2016.11.015.

[17] C. Ouellet-Plamondon, G. Habert, Life cycle assessment (LCA) of alkali-activated cements and concretes, in: F. Pacheco-Torgal, J. Labrincha, C. Leonelli, A. Palomo, P. Chindaprasit (Eds.), Handbook of Alkali-Activated Cements, Mortars and Concretes, Elsevier, Amsterdam, 2014, pp. 663–686.

[18] C.Y. Bai, P. Colombo, Processing, properties and applications of highly porous geopolymers: a review, Ceram. Int. 44 (14) (Oct 2018) 16103–16118, https://doi.org/10.1016/j.ceramint.2018.05.219.

[19] E. Prud'homme, E. Joussein, S. Rossignol, Use of silicon carbide sludge to form porous alkali-activated materials for insulating application, Eur. Phys. J. Spec. Top. 224 (9) (Jul 2015) 1725–1735, https://doi.org/10.1140/epjst/e2015-02494-7.

[20] P.R. Rao, K. Muralidharan, M. Momayez, K.A. Runge, D.A. Loy, Direct foaming driven synthesis and thermophysical characterization of silica-alumina foams: applications for thermal insulation, Ceram. Int. 46 (8) (Jun 2020) 10431–10441, https://doi.org/10.1016/j.ceramint.2020.01.042.

[21] V. Ducman, L. Korat, Characterization of geopolymer fly-ash based foams obtained with the addition of Al powder or H2O2 as foaming agents, Mater. Char. 113 (Mar 2016) 207–213, https://doi.org/10.1016/j.matchar.2016.01.019.

[22] L. Korat, V. Ducman, The influence of the stabilizing agent SDS on porosity development in alkali-activated fly-ash based foams, Cement Concr. Compos. 80 (Jul 2017) 168–174, https://doi.org/10.1016/j.cemconcomp.2017.03.010.

[23] Z.H. Zhang, J.L. Provis, A. Reid, H. Wang, Geopolymer foam concrete: an emerging material for sustainable construction, Construct. Build. Mater. 56 (Apr 2014) 113–127, https://doi.org/10.1016/j.conbuildmat.2014.01.081.

[24] A. Hajimohammadi, T. Ngo, P. Mendis, Enhancing the strength of pre-made foams for foam concrete applications, Cement Concr. Compos. 87 (Mar 2018) 164–171, https://doi.org/10.1016/j.cemconcomp.2017.12.014.

[25] C.Y. Bai, T. Ni, Q.L. Wang, H.Q. Li, P. Colombo, Porosity, mechanical and insulating properties of geopolymer foams using vegetable oil as the stabilizing agent, J. Eur. Ceram. Soc. 38 (2) (Feb 2018) 799–805, https://doi.org/10.1016/j.jeurceramsoc.2017.09.021.

[26] V. Medri, et al., Production and characterization of lightweight vermiculite/geopolymer-based panels, Mater. Des. 85 (Nov 2015) 266–274, https://doi.org/10.1016/j.matdes.2015.06.145.

[27] A. Hajimohammadi, T. Ngo, P. Mendis, T. Nguyen, A. Kashani, J.S.J. van Deventer, Pore characteristics in one-part mix geopolymers foamed by H2O2: the impact of mix design, Mater. Des. 130 (Sep 15 2017) 381–391, https://doi.org/10.1016/j.matdes.2017.05.084.

[28] J.D. Wu, Z.R. Zhang, Y. Zhang, D.X. Li, Preparation and characterization of ultra-lightweight foamed geopolymer (UFG) based on fly ash-metakaolin blends, Construct. Build. Mater. 168 (Apr 2018) 771–779, https://doi.org/10.1016/j.conbuildmat.2018.02.097.

[29] H. Cheng-Yong, L. Yun-Ming, M.M.A. Abdullah, K. Hussin, Thermal resistance variations of fly ash geopolymers: foaming responses, Sci. Rep. 7 (Mar 2017), https://doi.org/10.1038/srep45355. Art no. 45355.

[30] P.K. Sarker, S. Kelly, Z.T. Yao, Effect of fire exposure on cracking, spalling and residual strength of fly ash geopolymer concrete, Mater. Des. 63 (Nov 2014) 584–592, https://doi.org/10.1016/j.matdes.2014.06.059.

[31] H.Y. Zhang, V. Kodur, L. Cao, S.L. Qi, Fiber reinforced geopolymers for fire resistance applications, in: International Conference on Performance-Based Fire and Fire Protection Engineering vol. 71, Icpffpe, 2013, pp. 153–158, https://doi.org/10.1016/j.proeng.2014.04.022.

[32] H.Y. Zhang, V. Kodur, S.L. Qi, L. Cao, B. Wu, Development of metakaolin-fly ash based geopolymers for fire resistance applications, Construct. Build. Mater. 55 (Mar 2014) 38–45, https://doi.org/10.1016/j.conbuildmat.2014.01.040.

[33] M. Lahoti, K.K. Wong, E.H. Yang, K.H. Tan, Effects of Si/Al molar ratio on strength endurance and volume stability of metakaolin geopolymers subject to elevated temperature, Ceram. Int. 44 (5) (Apr 2018) 5726–5734, https://doi.org/10.1016/j.ceramint.2017.12.226.

[34] F.H. Fan, Z. Liu, G.J. Xu, H. Peng, C.S. Cai, Mechanical and thermal properties of fly ash based geopolymers, Construct. Build. Mater. 160 (Jan 2018) 66–81, https://doi.org/10.1016/j.conbuildmat.2017.11.023.

[35] M. Guerrieri, J. Sanjayan, F. Collins, Residual strength properties of sodium silicate alkali activated slag paste exposed to elevated temperatures, Mater. Struct. 43 (6) (Jul 2010) 765–773, https://doi.org/10.1617/s11527-009-9546-3.

[36] Z.H. Zhang, J.L. Provis, A. Reid, H. Wang, Mechanical, thermal insulation, thermal resistance and acoustic absorption properties of geopolymer foam concrete, Cement Concr. Compos. 62 (Sep 2015) 97–105, https://doi.org/10.1016/j.cemconcomp.2015.03.013.

[37] O.A. Abdulkareem, M.M.A. Abdullah, K. Hussin, K.N. Ismail, M. Binhussain, Mechanical and microstructural evaluations of lightweight Aggregate geopolymer concrete before and after exposed to elevated temperatures, Materials 6 (10) (Oct 2013) 4450–4461, https://doi.org/10.3390/ma6104450.

[38] A.I. Badanoiu, T.H.A. Al Saadi, S. Stoleriu, G. Voicu, Preparation and characterization of foamed geopolymers from waste glass and red mud, Construct. Build. Mater. 84 (Jun 2015) 284–293, https://doi.org/10.1016/j.conbuildmat.2015.03.004.

[39] F. Skvara, R. Sulc, Z. Tisler, P. Skricik, V. Smilauer, Z.Z. Cilova, Preparation and properties OF fly ash-based geopolymer foams, Ceramics 58 (3) (2014) 188–197.

[40] P. Hlavacek, V. Smilauer, F. Skvara, L. Kopecky, R. Sulc, Inorganic foams made from alkali-activated fly ash: mechanical, chemical and physical properties, J. Eur. Ceram. Soc. 35 (2) (Feb 2015) 703–709, https://doi.org/10.1016/j.jeurceramsoc.2014.08.024.

[41] P. Duxson, J.L. Provis, G.C. Lukey, F. Separovic, J.S.J. van Deventer, 29Si NMR study of structural ordering in aluminosilicate geopolymer gels, Langmuir 21 (7) (2005) 3028–3036.

[42] P. Duxson, S.W. Mallicoat, G.C. Lukey, W.M. Kriven, J.S.J. van Deventer, The effect of alkali and Si/Al ratio on the development of mechanical properties of metakaolin-based geopolymers, Colloid. Surface. Physicochem. Eng. Aspect. 292 (1) (2007) 8–20, https://doi.org/10.1016/j.colsurfa.2006.05.044.

[43] L. Korat, V. Ducman, Characterization of fly ash alkali activated foams obtained using sodium perborate monohydrate as a foaming agent at room and elevated temperatures, Frontiers in Materials 7 (Sep 2020), https://doi.org/10.3389/fmats.2020.572347. Art no. 572347.

[44] K. Traven, M. Češnovar, S.D. Škapin, V. Ducman, Evaluation of fly ash based alkali-activated foams at room and elevated temperatures, in: International Conference on Technologies & Business Models for Circular Economy: Conference Proceedings, Portorož, Slovenia, 2020 presented at the 2nd, https://press.um.si/index.php/ump/catalog/view/472/570/801-1.

[45] P. Rovnanik, Effect of curing temperature on the development of hard structure of metakaolin-based geopolymer, Construct. Build. Mater. 24 (7) (Jul 2010) 1176–1183, https://doi.org/10.1016/j.conbuildmat.2009.12.023.

[46] K. Traven, M. Češnovar, S.D. Škapin, V. Ducman, Mechanical and microstructural properties of fly ash-based alkali-activated foams exposed to room and elevated temperatures, in: 74th RILEM Annual Week & the 40th Cement and Concrete Science Conference, Sheffield, United Kingdom, 2020. https://www.sheffield.ac.uk/materials/rilem2020/programme.

[47] EN 196-2 – Method of Testing Cement – Part 2, Chemical Analysis of Cement, 2013.

[48] *DIN EN 196-1 – Methods Of Testing Cement - Part 1: Determination Of Strength*, 2016.

[49] P. Duxson, G.C. Lukey, J.S.J. van Deventer, The thermal evolution of metakaolin geopolymers: Part 2 - phase stability and structural development, J. Non-Cryst. Solids 353 (22–23) (Jul 2007) 2186–2200, https://doi.org/10.1016/j.jnoncrysol.2007.02.050.

[50] M.K. Lahoti, K.H. Tan, E.H. Yang, A critical review of geopolymer properties for structural fire-resistance applications, Construct. Build. Mater. 221 (Oct 2019) 514–526, https://doi.org/10.1016/j.conbuildmat.2019.06.076.

[51] W.D.A. Rickard, A. van Riessen, P. Walls, Thermal character of geopolymers synthesized from class F fly ash containing high concentrations of iron and alpha-quartz, Int. J. Appl. Ceram. Technol. 7 (1) (2010) 81–88, https://doi.org/10.1111/j.1744-7402.2008.02328.x.

[52] J.L. Provis, R.M. Harrex, S.A. Bernal, P. Duxson, J.S.J. van Deventer, Dilatometry of geopolymers as a means of selecting desirable fly ash sources, J. Non-Cryst. Solids 358 (16) (Aug 2012) 1930–1937, https://doi.org/10.1016/j.jnoncrysol.2012.06.001.

[53] M. Lahoti, K.K. Wong, K.H. Tan, E.H. Yang, Effect of alkali cation type on strength endurance of fly ash geopolymers subject to high temperature exposure, Mater. Des. 154 (Sep 2018) 8–19, https://doi.org/10.1016/j.matdes.2018.05.023.

[54] H.F. Shermer, Thermal expansion of binary alkali silicate glasses, J. Res. Natl. Bur. Stand. 57 (1956) 97–101. https://nvlpubs.nist.gov/nistpubs/jres/057/jresv57n2p97_A1b.pdf.
[55] A.J. Steveson, W.M. Kriven, Tailorable thermal expansion in leucite-pollucite materials derived from geopolymers for environmental barrier coatings, J. Am. Ceram. Soc. 104 (2021) 3397–3410, https://doi.org/10.1111/jace.17630.
[56] Geopolymers, Structures, Processing, Properties and Industrial Applications, in: first ed., in: J. Provis, J.S.J. van Deventer (Eds.), Woodhead Publishing Series in Civil and Structural Engineering, 2009, pp. 315–342 (chapter 15) (Thermal properties of geopolymers).
[57] T. Bakharev, Thermal behaviour of geopolymers prepared using class F fly ash and elevated temperature curing, Cement Concr. Res. 36 (6) (2006) 1134–1147, https://doi.org/10.1016/j.cemconres.2006.03.022.
[58] E. Prud'homme, P. Michaud, E. Joussein, J.M. Clacens, S. Rossignol, Role of alkaline cations and water content on geomaterial foams: monitoring during formation, J. Non-Cryst. Solids 357 (4) (Feb 2011) 1270–1278, https://doi.org/10.1016/j.jnoncrysol.2010.12.030.
[59] O.G. Rivera, et al., Effect of elevated temperature on alkali-activated geopolymeric binders compared to portland cement-based binders, Cement Concr. Res. 90 (Dec 2016) 43–51, https://doi.org/10.1016/j.cemconres.2016.09.013.
[60] D.D.B. Nergis, M.M.A. Abdullah, A.V. Sandu, P. Vizureanu, XRD and TG-DTA study of new alkali activated materials based on fly ash with sand and glass powder, Materials 13 (2) (Jan 2020), https://doi.org/10.3390/ma13020343. Art no. 343.
[61] W.D.A. Rickard, J. Temuujin, A. van Riessen, Thermal analysis of geopolymer pastes synthesised from five fly ashes of variable composition, J. Non-Cryst. Solids 358 (15) (Aug 2012) 1830–1839, https://doi.org/10.1016/j.jnoncrysol.2012.05.032.
[62] P.G. He, D.C. Jia, S.J. Wang, Microstructure and integrity of leucite ceramic derived from potassium-based geopolymer precursor, J. Eur. Ceram. Soc. 33 (4) (Apr 2013) 689–698, https://doi.org/10.1016/j.jeurceramsoc.2012.10.019.
[63] W.D.A. Rickard, L. Vickers, A. van Riessen, Performance of fibre reinforced, low density metakaolin geopolymers under simulated fire conditions, Appl. Clay Sci. 73 (Mar 2013) 71–77, https://doi.org/10.1016/j.clay.2012.10.006.
[64] K. Dombrowski, A. Buchwald, M. Weil, The influence of calcium content on the structure and thermal performance of fly ash based geopolymers, J. Mater. Sci. 42 (9) (May 2007) 3033–3043, https://doi.org/10.1007/s10853-006-0532-7.
[65] G.R. Qian, Y. Song, C.G. Zhang, Y.Q. Xia, H.H. Zhang, P.C. Chui, Diopside-based glass-ceramics from MSW fly ash and bottom ash, Waste Manag. 26 (12) (2006) 1462–1467, https://doi.org/10.1016/j.wasman.2005.12.009.
[66] E. Prud'homme, et al., Structural characterization of geomaterial foams - thermal behavior, J. Non-Cryst. Solids 357 (21) (Nov 2011) 3637–3647, https://doi.org/10.1016/j.jnoncrysol.2011.06.033.